ACS NANO

ARTICLE

Tumor Targeting by $\alpha_v\beta_3$-Integrin-Specific Lipid Nanoparticles Occurs *via* Phagocyte Hitchhiking

Alexandros Marios Sofias,* Yohana C. Toner, Anu E. Meerwaldt, Mandy M. T. van Leent, Georgios Soultanidis, Mattijs Elschot, Haruki Gonai, Kristin Grendstad, Åsmund Flobak, Ulrike Neckmann, Camilla Wolowczyk, Elizabeth L. Fisher, Thomas Reiner, Catharina de Lange Davies, Geir Bjørkøy, Abraham J. P. Teunissen, Jordi Ochando, Carlos Pérez-Medina, Willem J. M. Mulder, and Sjoerd Hak*

Cite This: *ACS Nano* 2020, 14, 7832−7846

Read Online

ACCESS | Metrics & More | Article Recommendations | Supporting Information

ABSTRACT: Although the first nanomedicine was clinically approved more than two decades ago, nanoparticles' (NP) *in vivo* behavior is complex and the immune system's role in their application remains elusive. At present, only passive-targeting nanoformulations have been clinically approved, while more complicated active-targeting strategies typically fail to advance from the early clinical phase stage. This absence of clinical translation is, among others, due to the very limited understanding for *in vivo* targeting mechanisms. Dynamic *in vivo* phenomena such as NPs' real-time targeting kinetics and phagocytes' contribution to active NP targeting remain largely unexplored. To better understand *in vivo* targeting, monitoring NP accumulation and distribution at complementary levels of spatial and temporal resolution is imperative. Here, we integrate *in vivo* positron emission tomography/computed tomography imaging with intravital microscopy and flow cytometric analyses to study $\alpha_v\beta_3$-integrin-targeted cyclic arginine-glycine-aspartate decorated liposomes and oil-in-water nanoemulsions in tumor mouse models. We observed that ligand-mediated accumulation in cancerous lesions is multifaceted and identified "NP hitchhiking" with phagocytes to contribute considerably to this intricate process. We anticipate that this understanding can facilitate rational improvement of nanomedicine applications and that immune cell−NP interactions can be harnessed to develop clinically viable nanomedicine-based immunotherapies.

KEYWORDS: *nanomedicine, cyclic RGD nanoparticles, immune cell hitchhiking, neutrophils, positron emission tomography/computed tomography imaging, intravital microscopy*

Tumor targeting by cRGD-nanoparticles occurs *via* phagocyte hitchhiking
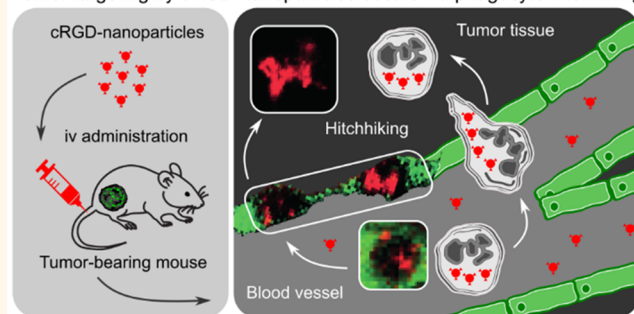
For medical purposes, *in vivo* nanoparticle (NP) application has become an enormous field with stakeholders ranging from individual patients to academics and large pharmaceutical corporations. Administration of drugs encapsulated in NPs can reduce systemic exposure and increase drug levels at pathological sites. Although these attractive features allowed for the first passive-targeting nanomedicine to be clinically approved more than two decades ago,[1] the lack of an in depth understanding of NP *in vivo* behavior remains one of the barriers for their widespread clinical use.[2−4]

One aspect of NP *in vivo* behavior that has largely been neglected, especially for ligand-decorated formulations, is the role of the immune system and its cells in NP targeting.[5−7] The immune system has evolved to protect its host from infections and comprises two arms: innate and adaptive immunity. Innate immunity is an ancient first-line host-defense system that primarily consists of phagocytes. These
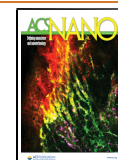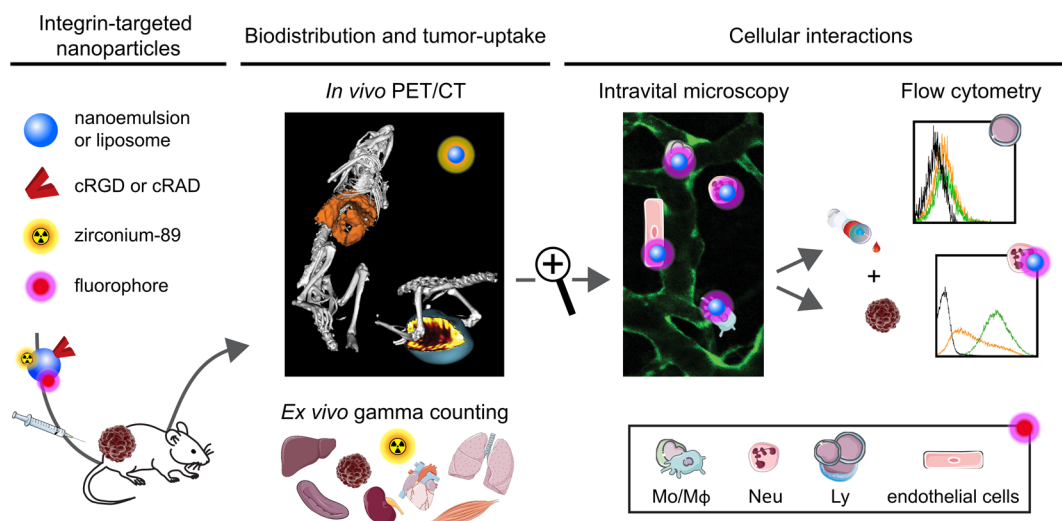
Figure 1. Study outline. Tumor-bearing mice were intravenously injected with [89]Zr- or fluorophore-labeled NPs, of which the pharmacokinetics, biodistribution, and accumulation in organs were quantified using positron emission tomography imaging and *ex vivo* gamma counting. NP interactions with cells were assessed with intravital confocal microscopy of tumors and *ex vivo* flow cytometry of blood and tumor single cell suspensions. Abbreviations: Mo/Mφ: monocytes/macrophages, Neu: neutrophils, Ly: lymphocytes.

cells are present in all tissues and have the capacity to rapidly, but nonspecifically, recognize and engulf foreign materials, such as nanomedicines. Upon its saturation, adaptive immunity, a more sophisticated and evolutionary modern part of the immune system, mounts a highly specific immune response and builds immunological memory. Here, we attempted to explore the immune system's roles in NP *in vivo* behavior, with a particular focus on phagocytes' contribution to active NP targeting.

As NP-targeting ligand, we selected cyclic arginine-glycine-aspartate (cRGD), which is one of the most widely used NP ligands in the field.[8] This is a ligand for $\alpha_v\beta_3$-integrin, which is upregulated on activated/angiogenic tumor vascular endothelium and several types of cancer cells.[8−10] Even though more than 500 preclinical studies (source: scopus.com) and 55 clinical trials (source: clinicaltrials.gov) have attempted to establish nanoformulations containing the RGD motif, their clinical utilization remains zero. Preclinically, the targeting abilities of cRGD-NPs, as well as from other ligand-decorated nanomedicine, are mainly assessed *in vitro*, *ex vivo*, or with macroscopic *in vivo* imaging modalities.[11,12] This kind of data provides little insight into *in vivo* targeting dynamics, mechanisms, and potential contributions of phagocytes. Although some studies include techniques that could provide mechanistic and real-time information on the microscopic level, observations are typically limited to static "snapshots" rather than continuous dynamic tracking.[13,14]

These realizations were our incentive for investigating real-time the fate of two $\alpha_v\beta_3$-integrin-targeted lipidic NP platforms in tumor mouse models using *in vivo* positron emission tomography/computed tomography (PET/CT) imaging integrated with intravital microscopy (IVM) and flow cytometry (Figure 1 provides the study outline). Particular attention was given to the full exploration of real-time NP targeting kinetics and their specific interactions with the circulating and tumor-homing immune system. We observed that ligand-mediated NP accumulation in cancerous lesions is multifaceted and identified "NP hitchhiking" with phagocytes to contribute considerably to this intricate process.

We anticipate that these insights will facilitate rational improvements of nanomedicine applications.

RESULTS AND DISCUSSION

Nanoparticles. Since approximately half of the clinically approved nanomedicines are lipid-based formulations,[15,16] we chose to study liposomes[17] (100 nm) and oil-in-water nanoemulsions[18] (150 nm). The lipid composition is very similar to that of the clinically approved Doxil.[19] We surface-functionalized these NPs with $\alpha_v\beta_3$-integrin-specific cyclic arginine-glycine-aspartate peptides (c[RGDfK], abbreviated as cRGD).[20] This peptide is not only one of the most widely studied targeting ligands (illustrated by both older[14,21] and recent publications[22−24]) but also one of the few NP-targeting ligands that has been tested in patients.[25−27] As a nonspecific control peptide, we used cyclic arginine-alanine-aspartate peptides (c[RADfK], abbreviated as cRAD).[28] Figure S1a provides the NP characterization data.

Biodistribution and Tumor Uptake. We first quantitatively studied NP *in vivo* behavior at the macroscopic level using a combination of *in vivo* PET/CT imaging and *ex vivo* gamma counting of blood fractions and organs after intravenous administration of zirconium-89 ([89]Zr)-labeled NPs to immunocompetent BALB/c mice bearing orthotopic 66cl4 tumors (murine mammary carcinoma). Contrary to the intuitive assumption that active targeting universally increases accumulation at target sites, cRGD-NPs' shorter blood circulation half-lives (Figure S1b) and concomitant increased liver and especially spleen uptake (as compared to cRAD-decorated analogues) diminished their targeting toward tumors (Figure 2a−c, Figures S2, S3, and S4a).

We observed that nonspecific cRAD-NPs accumulate throughout the tumors (Figure 2d), facilitated by the homogeneous vascularization of our tumor model (Figure S4b,c) and enhanced endothelial permeability. cRGD-NPs' tumor distribution pattern, especially their accumulation kinetics, was strikingly different. In the first hour following their intravenous injection, $\alpha_v\beta_3$-integrin-specific cRGD-NPs were found predominantly in the tumor periphery (Figure 2d,e and Figure S4d,e), a pattern we observed previously in
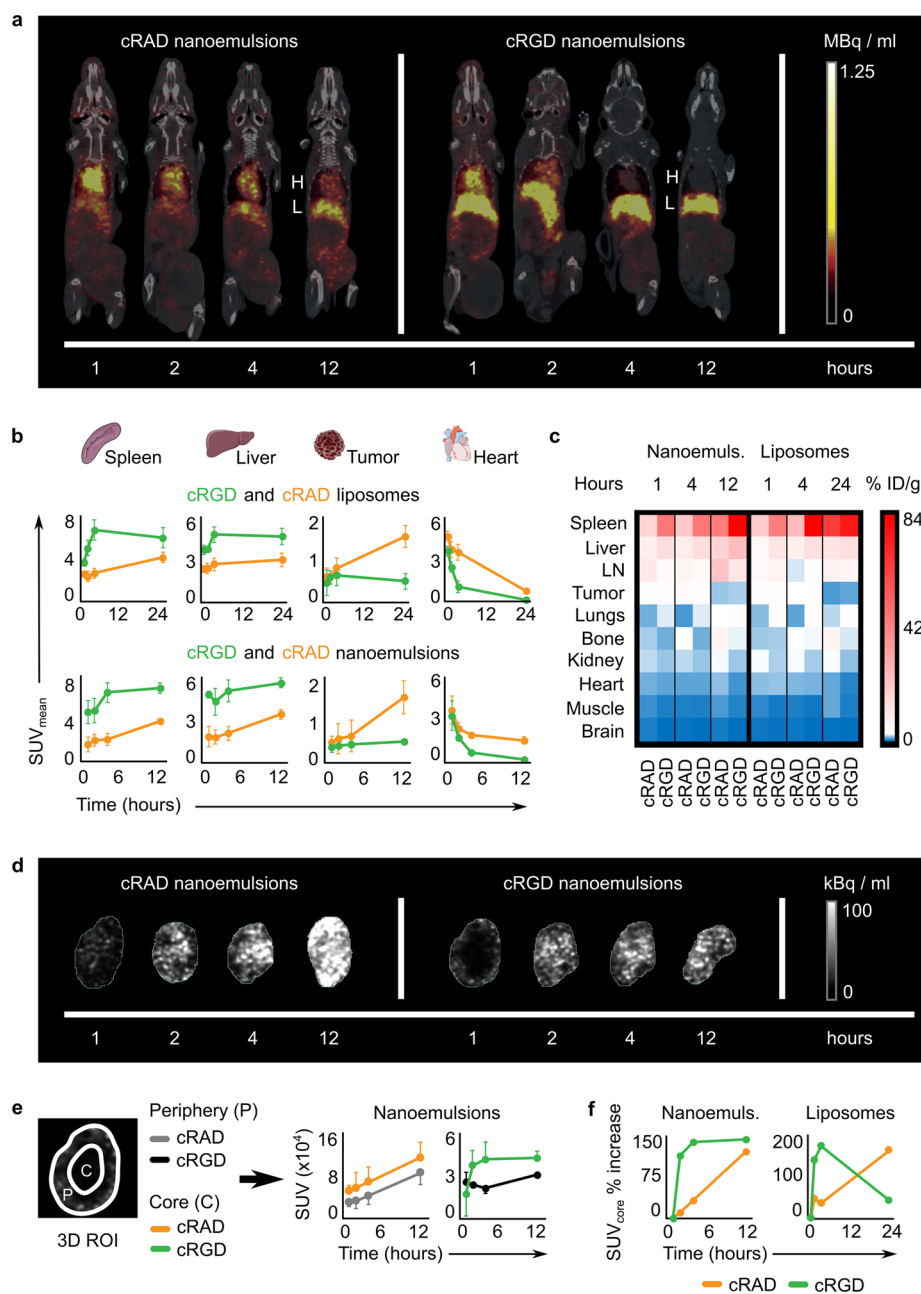
Figure 2. PET/CT imaging and gamma counting. (a) PET/CT images of mice injected with cRAD or cRGD nanoemulsions (liposomes in Figure S4a). Compared to cRAD-NPs, cRGD-NPs cleared faster (Figure S1b), as evidenced by more rapid signal decrease in the heart (H), and accumulated to higher extent in the liver (L). (b) Mean SUV as a function of time for spleen, liver, tumor, and heart. cRGD-NPs accumulated to higher extent in liver and spleen, whereas cRAD-NPs reached higher levels in tumors. Signal from the heart reflects the differences in circulation half-lives; $n = 4-6$ per formulation per time point. (c) A heatmap of NP biodistribution profiles obtained with *ex vivo* gamma counting on isolated organs corroborated the PET/CT imaging (the heatmap is created based on the data in Figures S2 and S3). (d) *In vivo* PET images of tumors showing homogeneous cRAD-NP accumulation at all time-points. At 1 h post-injection, cRGD-nanoemulsions (liposomes in Figure S4d) were mainly found in the tumor periphery. (e) Tumor SUV as a function of time in the core and periphery after cRAD-NP or cRGD-nanoemulsions ($n = 4$ per formulation per time point) administration (liposomes in Figure S4e). (f) SUV increase in the tumor core, relative to the SUV at 1 h post-injection, as a function of time. From 1 to 4 h post-injection, the cRGD-NP distribution pattern shifted from the lesion periphery to the tumor core at a much more rapid rate than cRAD-NPs. Error bars in (b) and (e): SD.

various tumor models *via* magnetic resonance imaging for cRGD-liposomes,[29] cRGD-nanoemulsions,[30] and cRGD-quantum dots.[31] Moreover, in a patient with liver metastasis, cRGD-conjugated silica NPs accumulated in the tumor margin as well.[27] Interestingly, between 1 and 4 h post-injection, the cRGD-NP distribution shifted rapidly from the tumor

periphery to its core, which we did not observe for cRAD-NPs in the same time frame (Figure 2e,f and Figure S4e). cRAD-NPs accumulated in the tumor core and periphery at similar rates (Figure 2e). cRGD-NPs however accumulated much faster in the core than in the periphery in the 1–4 h time frame (Figure 2e). Moreover, the relative accumulation
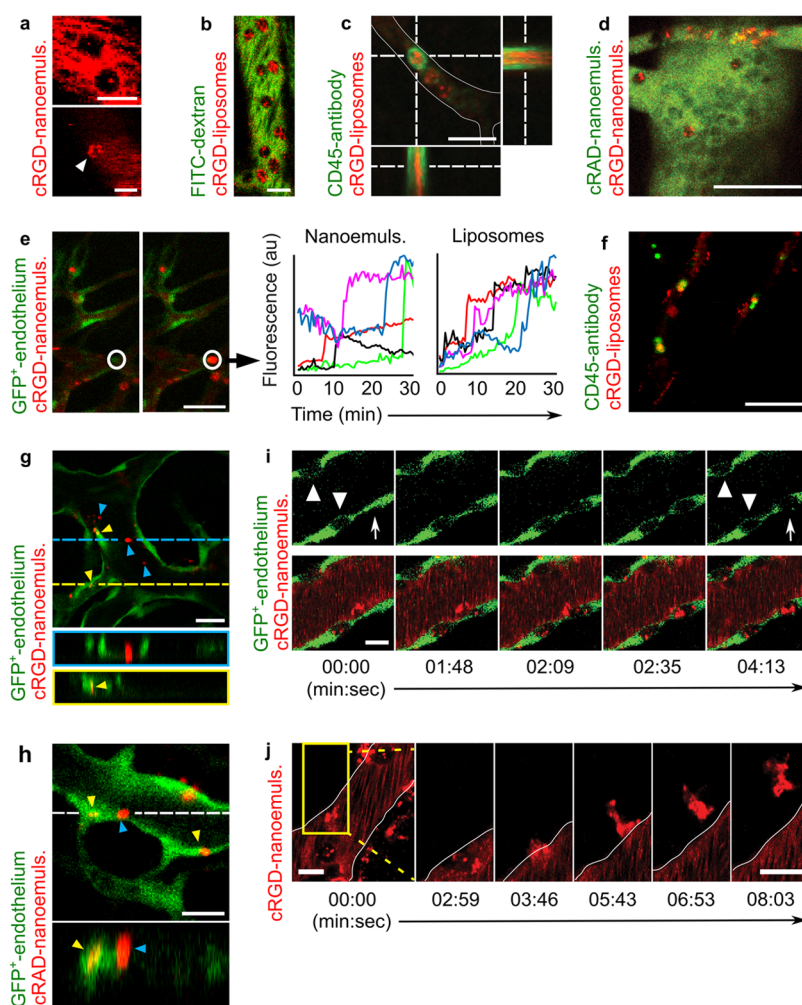
Figure 3. Intravital microscopy of tumors. (a) cRGD-nanoemulsions (red) agglomerates with ring-like appearances (arrowhead) and inside circulating "black holes" 15 min post-injection. (b) This phenomenon was especially apparent when FITC-Dextran (green) was coinjected with cRGD-liposomes (red, 3 h post-injection). (c) Intravital CD45-staining (green) confirmed that circulating immune cells internalize cRGD-liposomes (red, 6 h post-injection). (d) Co-injections demonstrated higher cellular uptake of cRGD-nanoemulsions (red) than cRAD-nanoemulsions (green) (35 min post-injection). (e) Frames of an imaging sequence showing a cRGD-nanoemulsion-positive cell (red) binding to tumor vasculature (green, GFP), indicated with a white region of interest (ROI). In NP fluorescence *versus* time graphs originating from such ROIs, "cell binding events" appeared as steps, further demonstrating that this binding did not result from gradual cRGD-NP accumulation. (f) A significant portion of accumulated cRGD-liposomes (red) presented in CD45$^+$ (green) cells (6 h post-injection). (g) Z-stack with $x-z$ projections showing a part of cRGD-nanoemulsions (red, 24 h post-injection) to colocalize with endothelium (green, GFP), indicative of targeting (yellow arrowheads). A considerable portion of the cRGD-nanoemulsions was present in nonendothelial agglomerates (GFP negative, blue arrowheads). cRGD-liposomes in Figure S6a. (h) A portion of cRAD-nanoemulsions (red, cRAD-liposomes in Figure S6b,c) was also taken up by endothelium. (i) Frames of an imaging sequence (1.5 h post-injection) showing "black holes" (arrowheads) in the endothelium (green, GFP), positive for cRGD-nanoemulsions (red). A cRGD-nanoemulsion-positive cell entering endothelium can also be appreciated (arrow). (j) Frames of an imaging sequence showing extravasation (from an outlined vessel) of cRGD-nanoemulsion-containing cells (3 h post-injection). Scale bars: (a−c, h−j) 10 μm, (d) 50 μm, and (e−g) 25 μm.

rate in the core was also faster for cRGD-NPs than for cRAD-NPs (Figure 2f). Since the cRGD-NP levels in the circulation drop rapidly in this time frame, tumors were homogeneously vascularized, and the control cRAD-NPs accumulated homogeneously throughout the tumor, this tumor accumulation pattern cannot be explained by endothelium targeting or vascular extravasation of the cRGD-NPs. Since we suspected this phenomenon was related to interactions with migrating immune cells, we next studied both lipid NPs' *in vivo* behavior at the cellular level using a combination of real-time IVM and flow cytometry.

Cellular Interactions Studied with Intravital Microscopy. To study cellular interactions in real-time, we performed high temporal and subcellular resolution IVM on 66cl4 tumors grown either in dorsal window chambers on immunodeficient TieGFP mice or orthotopically in immunocompetent Tie2GFP mice.[32] IVM showed that both cRGD liposomes and nanoemulsions behaved in a similar manner (Figure 3). Nevertheless, the identified patterns were strikingly different in comparison to their control-analogues cRAD liposomes and nanoemulsions. Within minutes after injection, we observed strong indications for cRGD-NP uptake by circulating immune cells (Figure 3a,b, Movies S1 and S2), which was confirmed by intravital CD45 (a membrane glycoprotein present on all leukocytes) staining (Figure 3c and Movie S3). During the first hour, we observed
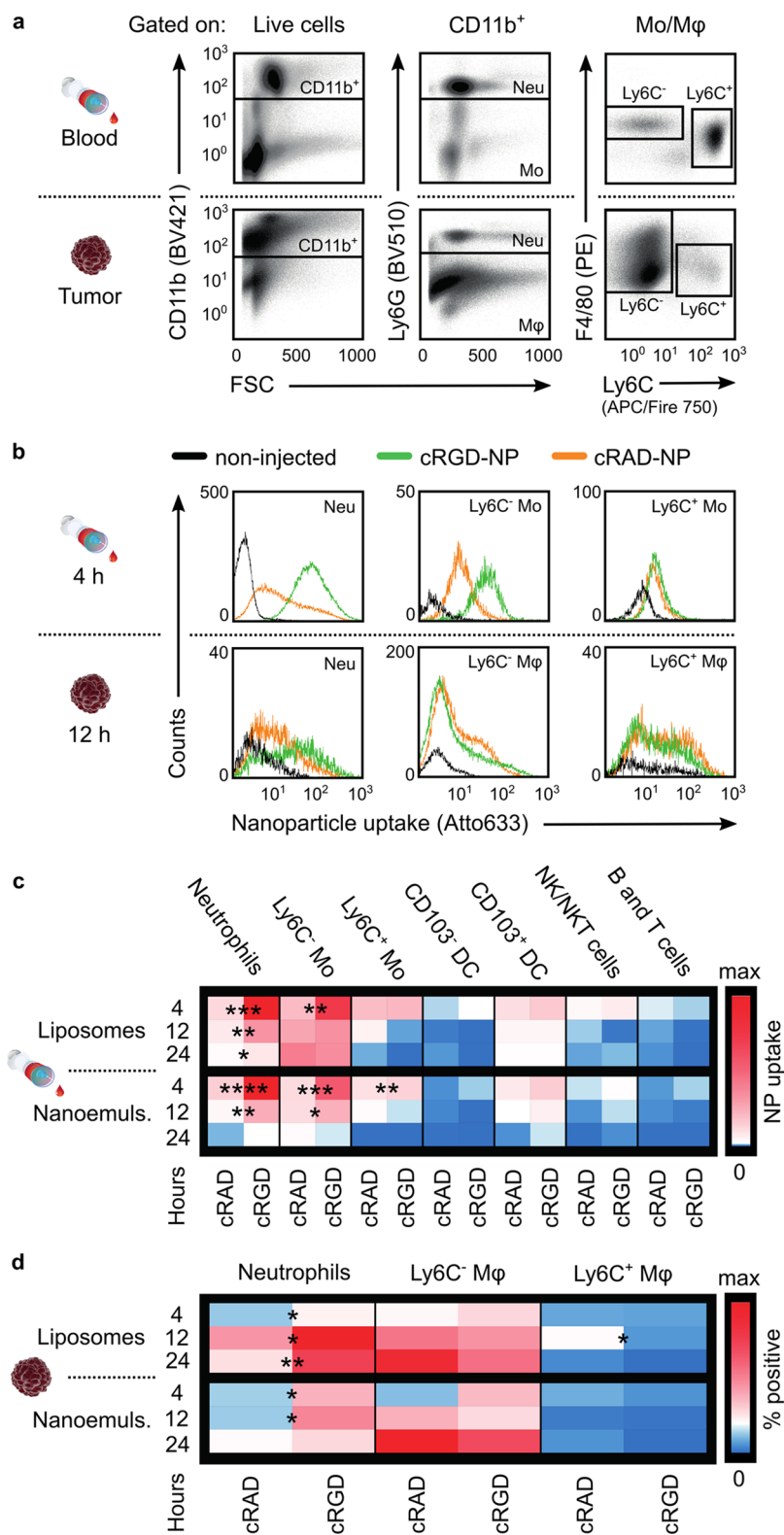
Figure 4. Flow cytometry analysis of blood and tumor. (a) Gating strategy for myeloid cells (full gating strategy in **Figure S7**). (b) Representative histograms showing NP uptake by neutrophils (Neu), alternatively activated Ly6C⁻ monocytes/macrophages (Mo/Mφ), and classically activated Ly6C⁺ Mo/Mφ in blood (4 h) and tumor (12 h). In blood, cRGD-NPs were taken up predominantly by neutrophils and Ly6C⁻ monocytes, and in tumors, neutrophils were the main contributor to cRGD-NP uptake (also see **Figure S8**). (c) Heatmap of liposomes and nanoemulsion uptake (median fluorescence intensity) in blood (*n* = 3−6 per formulation per time point). The highest uptake was observed in neutrophils and monocytes, which also showed significant preference for cRGD-NPs. Also see **Figure S9a**. (d) Heatmap of NP uptake (*n* = 3−6 per formulation per time point) by tumor-associated phagocytes. Four h post-injection, more neutrophils and Ly6C- macrophages contained cRGD- than cRAD-NPs. At later time-points, this was still the case for neutrophils, whereas more Ly6C- macrophages contained cRAD- than cRGD-NPs (also see **Figure S9b**). *P*-values: * <0.05, ** <0.01, *** <0.001, **** <0.0001.

negligible cRAD-NP leukocyte uptake (Movies S4 and S5). This pattern persisted up to 24 h post-injection, with extensive cRGD-NP cellular uptake (Movies S6 and S7) and some, but significantly fewer, cRAD-NP positive circulating leukocytes (Movies S8 and S9). We corroborated these observations by studying NP coinjections with IVM (Figure 3d and Movies S10 and S11) as well as *ex vivo* microscopy on isolated leukocytes (Figure S5).

Interestingly, we observed cRGD-NP-positive cells (appearing as red clusters) to bind suddenly in the tumor vasculature (Figure 3e). By designing region of interests (ROIs) around the spots where these "red clusters" appeared and plotting the NP fluorescence as a function of time, it became evident that the binding events were a result of sudden "targeting" of an entire cluster, rather than gradual accumulation/binding of individual cRGD-NPs (Figure 3e). The use of CD45 antibodies allowed us to verify the NPs' presence in blood vessel-associated CD45$^+$ immune cells (Figure 3c,f). Unexpectedly, but in accordance with the idea that immune cells play a significant role in cRGD-NP tumor targeting, only a fraction of accumulated cRGD-NPs were associated with (GFP-expressing) tumor blood vessel endothelial cells (Figure 3g and Figure S6a). Even more surprisingly, a small portion of accumulated cRAD-NPs directly associated with tumor vascular endothelium as well (Figure 3h and Figure S6b,c).

cRGD-NP-positive cells not only bound to the luminal endothelium but also interacted closely with (GFP-expressing) endothelial cells (Figure 3i). Finally, these cRGD-NP-loaded cells were observed to extravasate extensively into and migrate through the tumor tissue (Figure 3j, Movies S12−S16). This phenomenon, which was not observed for cRAD-NPs (Movie S17), demonstrates immune cells' critical role in cRGD-NPs' distribution through the tumor interstitium.

Cellular Interactions Studied with Flow Cytometry. The dynamic IVM in mice with endothelial GFP expression was pivotal for concluding that (CD45$^+$) leukocytes contribute considerably to cRGD-NP tumor targeting. Moreover, the IVM observation that nanoparticle-loaded cells migrate through the tumor interstitium may also explain the cRGD-NP redistribution from the tumor periphery to the core as observed with PET imaging. To determine which immune cells were involved, we performed flow cytometry on blood and tumor single cell suspensions at 4, 12, and 24 h after NP administration to immunocompetent BALB/c mice bearing orthotopic 66cl4 tumors. Facilitated by a comprehensive antibody panel, we identified the main phagocyte (myeloid-derived immune cell) populations: neutrophils (CD45$^+$CD11b$^+$Ly6G$^+$) and monocytes/macrophages (CD45$^+$CD11b$^+$Ly6G$^-$Ly6C$^-$F4/80$^+$ or CD45$^+$CD11b$^+$Ly6G$^-$Ly6C$^+$F4/80^{intermediate}).

Monocytes constitute 5−10% of circulating immune cells. Upon entering tissues, these cells differentiate into macrophages, a key function of which is to phagocytose pathogens and extracellular debris.[33] Depending on the cytokines in their surroundings, these phagocytes are subject to classical or alternative activation. Classically activated monocytes/macrophages (CD45$^+$CD11b$^+$Ly6G$^-$Ly6C$^+$F4/80^{intermediate}) usually fulfill pro-inflammatory functions, as during infection to fight pathogens. Tumor-associated macrophages (TAMs) (CD45$^+$CD11b$^+$Ly6G$^-$Ly6C$^-$F4/80$^+$) are typically alternatively activated, similar to macrophages in wound healing, and contribute to the local immune suppression in the tumor microenvironment.[33]

Neutrophils are by far the most abundant leukocyte in blood (50−70% of circulating immune cells). These phagocytes are produced at very high rates (more than 10^{11} per day in humans) and are constantly replenished at recruitment sites like inflamed tissues and solid tumors.[34] Largely due to their short lifespan, neutrophils have long been considered merely a first line of defense against infections, but are now recognized as important actors in cancer development and progression. Not unlike TAMs, neutrophils appear to play pivotal roles in tumor initiation, immune suppression, angiogenesis, and metastasis (as reviewed in refs 34 and 35).

Figure 4a illustrates the key gating strategy used to detect the three main phagocytic myeloid cell populations in blood and tumor single-cell suspensions. Additionally, we studied NP interactions with dendritic cells (CD11c$^+$CD103$^+$ or CD11c$^+$CD103$^-$), which are innate immune cells that shape adaptive immune responses by presenting antigens. Finally, we also defined the main lymphoid-derived cell populations comprising the adaptive immune system: natural killer (CD11b$^-$FSC^{low}SSC^{low}NK-1.1$^+$), T-, and B-cells (CD11b$^-$FSC^{low}SSC^{low}NK-1.1$^-$). Figure S7 describes the full gating strategy.

In blood, we observed extensive interactions between CD11b$^+$ myeloid cells and cRGD-NPs, which were predominantly found in Ly6G$^+$ neutrophils and Ly6G$^-$/Ly6C$^-$ alternatively activated monocytes (Figure 4b,c and Figures S8a,b and S9a). cRAD-NPs were found in the same cell populations (Figure 4b,c), but at significantly lower levels. We observed few interactions between either of the NPs and lymphocytes (Figure 4c and Figures S8a,b and S9a). This confirmed, as expected, that phagocytic myeloid cells extensively ingested intravenously administered NPs.

CD11b$^+$ myeloid cells made up 75% of the immune cells in 66cl4 breast tumors (Figure S10). We observed striking differences between cRGD- and cRAD-NP levels in the different myeloid cell populations. Although circulating monocytes/macrophages showed a significant preference for cRGD-NPs, TAMs tended to contain higher or similar amounts of nonspecific cRAD-NPs as compared to cRGD-NPs (Figure 4b,d and Figure S8c,d and S9b). In the context of cRAD-NPs' longer blood half-life and higher tumor uptake, this apparent TAM preference can be best explained by cRAD-NPs' extravasation (passive accumulation) into tumor tissue and their subsequent uptake by TAMs.

Interestingly, $\alpha_v\beta_3$-integrin-specific cRGD-NPs displayed a notable proclivity toward neutrophils in both blood and tumor (Figure 4c,d and Figure S8 and S9). This indicates that these cRGD-NPs actively associate with neutrophils in the blood before migrating to the tumor. These clear differences in NP presence in tumor-associated neutrophils and macrophages strongly suggest that neutrophils are the main phagocytic contributor to cRGD-NPs hitchhiking to the tumor. The short life span of neutrophils, which are highly motile cells,[36] requires their tumor infiltration to occur rapidly and continuously. These cellular features and our observations support the idea that neutrophils are indeed capable of NP delivery to tumors and intratumoral nanomaterial distribution.

Associating cRGD-Nanoparticle Uptake with $\alpha_v\beta_3$-Integrin Expression. The interesting observations obtained by IVM and flow cytometry revealed a clear preference of myeloid cells and especially neutrophils for cRGD-NPs. The staining of all main immune cell populations with α_v and β_3 integrin subunits revealed a high co-expression of these
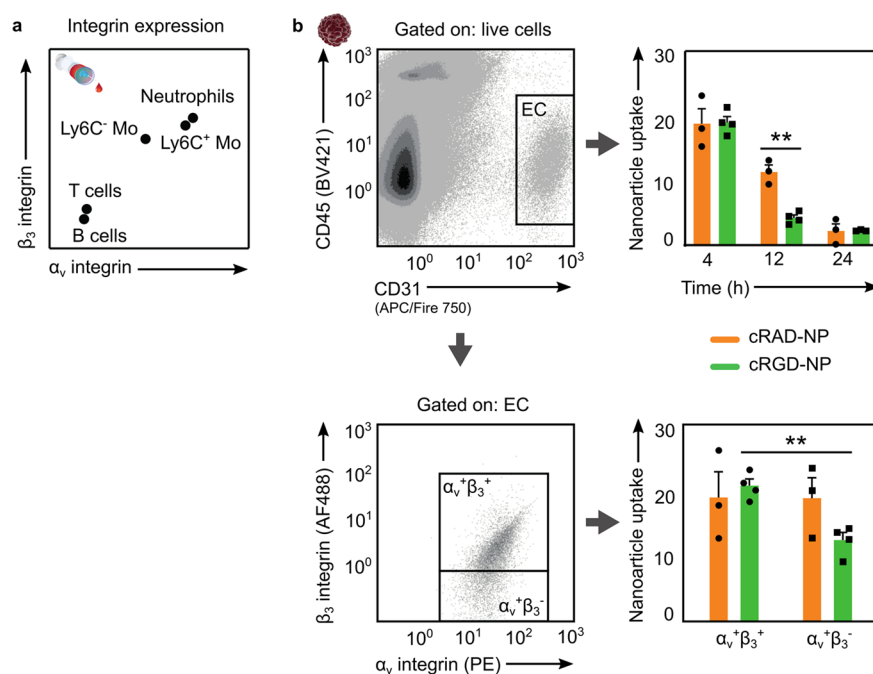
Figure 5. Association of nanoparticle uptake with α_v and $\beta_3$integrin. (a) Integrin co-expression for the key cell populations in blood, showing high α_v and β_3 integrin co-expression by myeloid cells (see also Figure S11). (b) In tumor, endothelial cells (EC) associated with cRAD-nanoemulsions (liposomes in Figure S12) similarly as (4 and 24 h) or even more than (12 h post-injection) with cRGD-NPs. However, significant differences in cRGD-NP uptake (median fluorescence intensity) by activated ($\alpha_v^+\beta_3^+$) and non-activated ($\alpha_v^+\beta_3^-$) cells were detected at 4 h post-injection. Error bars: Standard error of the mean. P-values: ** <0.01.

integrins by myeloid cells. Hence, the increased cRGD−NP interaction with phagocytes may be an effect of $\alpha_v\beta_3$-integrin expression (Figure 5a and Figure S11) on these cells.

Finally, in line with IVM observations, flow cytometry showed that cRGD- and cRAD-NPs were taken up by CD31^{+} endothelial cells to similar extents. However, as expected, cRGD-NPs showed a significant preference for activated endothelial cells, characterized by dual expression of both α_v and β_3 integrin subunits (Figure 5b and Figure S12).

General Discussion. Taken together, the distinctly detailed results from our complementary approach have here untangled phagocytes' contribution to active cRGD-decorated lipid NP tumor targeting. cRGD-NP accumulation kinetics in the tumor core, as observed by PET imaging, could not be explained by established vascular extravasation and direct endothelium targeting mechanisms. IVM showed that cRGD-NPs hitchhike with immune cells to the tumor vasculature. Moreover, these immune cells were found to extravasate and distribute the internalized nanomaterial into the tumor. Carefully designed flow cytometry experiments corroborated these findings and revealed neutrophils to be the main phagocytic contributor to this intricate process.

Interestingly, we also observed extensive uptake of cRGD-NPs in circulating immune cells in healthy Balb/c mice in a previous study.[37] Furthermore, in healthy tissue, these cRGD-NP loaded circulating immune cells behaved as can be expected; freely circulating as well as some of them rolling along the vessel wall.[38,39] However, no extravasating immune cells were observed (Figure S13 and Movies 18 and 19). Taken together this strongly suggests that the cRGD-NP uptake by myeloid cells occurs independent of cancer and that hitchhiking depends on (patho)physiological immune cell infiltration.

The difference between our study and older studies attempting to explain or exploit the cRGD-mediated targeting is that our highly complementary approach allowed for gaining information from macroscopic to submicron level. High spatial resolution IVM revealed cRGD-NP clusters bound to tumor vasculature (e.g., Figure 3g,h), which we[40] and others[13,41−44] have observed before and interpreted as cRGD−NP interaction with endothelium. The high IVM temporal resolution (0.2−0.3 s) we utilized allowed for recording very rapid events and detecting fluorescent clusters in the circulation that were not NP aggregates, but immune cells that had endocytosed cRGD-NP. Subsequent flow cytometric analysis enabled us not only to discover the extensive association between immune cells and cRGD-NPs but also to establish "immune cell hitchhiking" as an important mechanism through which tumor targeting of lipidic cRGD-NPs can be mediated.

Particularly for cRGD-NP, the contribution of myeloid cells and specifically neutrophils to tumor targeting has not been investigated before. However, interestingly, a few other studies also report myeloid cell proclivity for cRGD-decorated-liposomes as well as for 1200 nm iron oxide loaded vesicles and show this phenomenon may be used as a tool to permeate the blood brain barrier.[45,46] This establishes the important role of phagocytes in the in vivo behavior of a wide variety of cRGD-decorated lipidic systems. Furthermore, it is well established that decoration of polymeric/metal/lipidic NPs with cRGD or other ligands does not necessarily lead to an improved tumor targeting.[47−49] Although in these studies the role of the immune system was not specifically studied, we believe that a deep investigation into this aspect of the in vivo behavior of ligand-decorated nanomedicine might "revive" their in vivo utilization and allow for alternative in vivo applications.

Although we gained these insights into the cRGD-NP tumor targeting, additional methodologies must be developed to quantify the relative contribution of NP hitchhiking. Emerging disciplines like nanoinformatics[50] combined with computational advances may facilitate this.[51] For example, machine learning-based algorithms may be able to distill and attribute relevance to the different kinetic targeting processes from multidimensional data sets.[52]

cRGD-decorated NPs are extensively applied for therapeutic purposes aimed to deliver drugs to tumors and angiogenic vasculature.[8,21,53,54] First of all, we here demonstrate that in terms of total NP levels in the tumor, cRGD NPs could only "match" (at early time points post-injection only) but never "exceed" those of cRAD-NPs. Moreover, our results suggest that NP cRGD decoration will also result in elevated drug levels in both circulating and angiogenesis-associated phagocytes. This stresses the importance of a careful consideration of the pathological conditions in which cRGD-conjugated drug delivery systems may be useful as well as what kind of drugs to incorporate in such formulations. In the case of conventional cytostatic nanomedicines, cRGD decoration could actually reduce the amount of therapeutic agent ending up in the tumor and intensify adverse side effects such as neutropenia. Instead, the selection of an immunomodulatory payload that will aim to alter myeloid immune cells toward an antitumor phenotype[55] or to specifically inhibit an immune subpopulation[56] seems more appropriate.

Another widely studied application for cRGD-NPs is molecular imaging of tumor angiogenesis.[29,57−59] We here showed that the accepted mode of angiogenesis targeting with cRGD-NPs on which this application is based, namely direct binding to integrin positive endothelium, only holds partially. Nevertheless, several studies report good correlation between in vivo imaging readouts and microvessel density[29] or other ex vivo analysis.[58] It is well established that neutrophils and monocytes interact with activated endothelium and accumulate at inflamed and angiogenic sites. Hence, on typically used macroscopic imaging modalities like MRI, or PET, cRGD-NP accumulation with these phagocytes in angiogenic/inflamed tissues could still report quite accurately on angiogenic activity, explaining the relative success of preclinical cRGD-NP application for angiogenesis imaging.

A number of recent studies support the insight that phagocytes can affect NP in vivo performance considerably. TAMs have been shown to internalize nanodrugs, migrate to hypoxic tumor regions,[60] and release the drug payload to neighboring tumor cells.[6] Furthermore, neutrophil-facilitated migration of NPs from circulation has been observed in inflamed[61] and cancerous tissues.[5] Importantly, recent studies in cancer patients demonstrate that significant interactions between nanomedicines and monocytes affect nanodrug pharmacokinetics and pharmacodynamics.[62,63] Hence, as we here showed for cRGD-decorated lipid NPs, phagocytic immune cells can play a notable yet poorly understood role in nanodrug in vivo applications. To facilitate clinical translation of ligand-conjugated formulations, which despite enormous efforts has not yet occurred, and to increase nanomedicines' clinical utility in general, we consider thoroughly assessing NP in vivo behavior, as we have presented here, to be critically important. Possibly, screening of NP libraries composed of different types of NPs (particle size, composition, shape, surface chemistry, charge, and ligand decoration) may also contribute to stratify NPs for different applications including immune cell, vascular, and tumor delivery.[64]

CONCLUSIONS

To conclude, using an integrative approach combining highly complementary experimental tools, we studied the complex in vivo fate of cRGD-decorated NPs. We established "phagocyte hitchhiking" as an important mechanism for cRGD-NP active tumor targeting. This demonstrates that despite RGD-NPs' widespread use and enrollment in clinical trials, we have a lot left to learn about their in vivo behavior. From a broader perspective, we believe that thorough investigations into NP in vivo behavior, like we presented here, are important for the future of nanomedicine. The resulting understanding and insights into their interaction with and effects on the immune system will be pivotal in the development of improved in vivo applications. Finally, as immunotherapy continues its recent rise, harnessing immune cell−NP interactions can become a viable strategy for developing immunomodulating nanomedicines.

EXPERIMENTAL SECTION

Experimental Design. The objective of the current study was to obtain a detailed understanding of the role for phagocytes in ligand-mediated tumor targeting. To do so, we synthesized two different lipidic NPs conjugated with cRGD, a ligand widely used to target $\alpha_v\beta_3$-integrin expressed on activated tumor vasculature. To address cRGD-NPs' biodistribution and 66cl4 (murine mammary carcinoma) tumor targeting, we utilized in vivo PET imaging and ex vivo gamma counting. cRGD-NPs' interactions with phagocytes and other cells were assessed using real-time IVM and ex vivo flow cytometry on blood and tumor single cell suspensions. Figure 1 and Figure S14 provide a study outline and an overview over the number of animals used throughout the study, respectively.

Nanoparticle Materials. 1,2-Distearoyl-sn-glycero-3-phosphocholine (DSPC), cholesterol, and 1,2-distearoyl-sn-glycero-3-phosphoethanolamine-N-[methoxy(polyethylene glycol)-2000] (PEG2000-DSPE) were purchased from Avanti Polar Lipids, Inc. cRGD-PEG2000-DSPE and cRAD-PEG2000-DSPE were purchased from SyMO-Chem (Eindhoven, The Netherlands). Fluorescent lipids, 1,2-dioleoyl-sn-glycero-3-phosphoethanolamine labeled with Atto 633 (Atto633-DOPE) and 1,2-dipalmitoyl-sn-glycero-3-phosphoethanolamine-N-(lissamine rhodamine B sulfonyl) (Rho-PE) were purchased from Sigma-Aldrich and Avanti Polar Lipids, respectively. Soybean oil and solvents were purchased from Sigma-Aldrich.

Nanoparticle Synthesis. NPs, liposomes, and nanoemulsions were synthesized according to established methods[37,40] (Table S1). Liposomes consisted of DSPC:cholesterol:PEG2000-DSPE:X-PEG2000-DSPE (where X is cRGD or cRAD) at 62:33:4:1 molar ratios. For radiolabeling and fluorescent labeling, we, respectively, added 0.5 mol % DFO-DSPE and 0.2 mol % fluorescent lipid (Atto633-DOPE or Rhodamine-PE). To obtain nanoemulsions, identical lipid mixtures were used, and 2.5 mg of soybean oil per μmol of lipids was added. All lipids and oil (in case of nanoemulsions) were dissolved in 4:1 chloroform: methanol. The lipid mixture was dripped slowly into 2 mL of preheated phosphate buffered saline (PBS) of pH 7.4, at 70 °C, under vigorous stirring (700 rpm) upon which solvents evaporated. The obtained crude NPs were downsized using tip sonication (30 W and 20 kHz; 15 min/25% duty cycle for 20 μmol lipids for liposomes, and 25 min/50% duty cycle for 20 μmol lipids for nanoemulsions). NP size (diameter, nm), dispersity (Đ), and ζ potential (mV) were determined using dynamic light scattering (DLS, Malvern's Zetasizer Nano). Liposomes and nanoemulsions were 100 and 150 nm, respectively, with Đ < 0.15, and ζ potential around −20 and −30 mV, respectively (Figure S1a). NP suspension had a final lipid concentration of 10

mM, and in all experiments, mice received an intravenous lipid dose of 80 μmol per kg, resulting in injection volumes of approximately 200 μL.

Nanoparticle Radiolabeling. For the NP radiolabeling and the preparation of the phospholipid chelator DSPE-DFO, similar methods were used as previously described.[19,65,66] [89]Zr-oxalate was produced at Memorial Sloan Kettering Cancer Center (New York) on an EBCO TR19/9 variable-beam energy cyclotron (Ebco Industries Inc., BC, Canada) via the [89]Y(p,n)[89]Zr reaction and purified in accordance with previously reported methods to yield [89]Zr with a specific activity of 195−497 MBq/μg.[66] Activity measurements were made using a Capintec CRC-15R Dose Calibrator (Capintec, Ramsey, NJ). [89]Zr-oxalate was neutralized with aqueous Na_2CO_3 (1 M), added to a solution of 0.5 mol % DFO-bearing liposomes or nanoemulsions in PBS, and stirred at 37 °C for 2 h. The labeled NPs were separated from free [89]Zr using a PD-10 desalting column (GE Healthcare), with PBS as the eluent and collecting 0.5 mL fractions. The radiochemical yield was typically >90%. The fractions containing most activity (∼1.5−2.0 mL) were used for the experiments. These had a radiochemical purity of >98%, as determined by SEC radio-HPLC analyses performed on a Shimadzu system equipped with a Superdex 10/300 SEC column and a A Lablogic Scan-RAM radio-TLC/HPLC detector. A flow rate of 1 mL/min was used with demiwater as the eluent.

Animals. For PET/CT, gamma counting, histology, and flow cytometry experiments, about 200 female BALB/c mice aged 8−12 weeks were purchased from Janvier Laboratories or The Jackson Laboratory. For IVM, we crossbred STOCK Tg(TIE2GFP)287Sato/J mice (expressing green fluorescent protein in vascular endothelial cells, strain 003658, The Jackson Laboratory) and BALB/c nude mice (Foxn1nu/nu, Envigo). Obtained breeder pairs consisted of immunodeficient (Foxn1nu/nu) male TIE2GFP mice and immunocompetent TIE2GFP females (Foxn1nu/+, immunodeficient females do not reproduce). Mice were kept under pathogen-free conditions at 20 °C, 50−60% humidity, and 65 air changes per hour and were allowed food and water ad libitum. All procedures were approved by the Norwegian Animal Research Authorities (IVM and flow cytometry) or by the Institutional Animal Care and Use Committees of the Icahn School of Medicine at Mount Sinai (PET/CT and gamma counting).

Tumor Model. The 66cl4 cell line (derived from 4T1 murine mammary carcinoma) was obtained from Barbara Ann Karmanos Cancer Institute. The cells were cultured in DMEM (Lonza, BioWhittaker, BE-604F) supplemented with 10% fetal calf serum (FCS, Thermo Fischer Scientific, #10270-106), 2 mM L-glutamine (Lonza Group, DE-17−605E), and 50 U/mL penicillin-streptomycin (Thermo Fischer Scientific, Gibco, #15070-063). The cells were incubated at 37 °C with 5% CO_2.

All mice were orthotopically inoculated into the fourth mammary fat pad with 5 × 10^{6} 66cl4 cells in 50 μL of sterile NaCl. The tumor growth and weight were regularly monitored. Animals were used for experiments at 14−21 days post-inoculation when tumors had an approximate volume of 250 mm[3].

Window chambers were implanted on immunodeficient TIE2GFP female mice with similar procedures as previously reported.[67] The day after chamber implantation, 1.5 × 10^{6} 66cl4 cells were implanted in the chamber. 12−16 days post-chamber implantation, when tumors filled 30−90% of the window area, the animals were subjected to IVM experiments. For IVM on orthotopically grown tumors, we implanted 66cl4 cells in 50 μL 1:1 sterile NaCl/matrigel (734-1101, Corning) in immunocompetent TIE2GFP mice. The 66cl4 tumor model immunoprofiling, based on data collected from tumor single cells suspensions (n = 57), is given in Figure S10.

Gamma Counting Experiments. To determine pharmacokinetic profiles (Figure S1b), 20 female BALB/c mice bearing 66cl4 orthotropic tumors were administered NPs (80 μmol lipid per kg; 108.2 ± 2.7 μCi for liposomes, 45.5 ± 6.2 μCi for nanoemulsions; n = 5 per NP) via the lateral tail vein. At 1, 5, 30 min and 1, 2, 4, 6, 12/24 h, about 5 μL of blood was collected from a small incision in the lateral tail vein. The blood samples were placed in preweighed

polystyrene gamma-counting tubes and gamma counted using a Wizard2 1-Detector Gamma Counter, PerkinElmer. The obtained gamma counts were plotted as%ID/g versus time, and the circulation half-life values were determined via monoexponential fitting with Matlab.

To determine NP biodistribution profiles, 60 female BALB/c mice bearing 66cl4 orthotropic tumors received NPs (80 μmol lipid per kg; 104.2 ± 7.8 μCi for liposomes, 53.8 ± 7.9 μCi for nanoemulsions; n = 15 per NP) via the lateral tail vein. At 1, 4, 12 h for nanoemulsions or 1, 4, 24 h for liposomes (n = 4−6 per NP per time point), mice were sacrificed, and 0.5−1 mL of blood was collected via heart puncturing. Then, all mice were perfused with PBS (10−15 mL) until all blood was visibly perfused out of liver and kidneys. Tumor, liver, spleen, kidneys, brain, bone, muscle, celiac lymph nodes, lungs, and heart were collected from each animal and placed in preweighted polystyrene gamma-counting tubes. The activity from each organ was determined by using a Wizard2 1-Detector Gamma Counter, PerkinElmer. Analysis of gamma counts revealed the biodistribution profile for all four NPs at three time points (Figure 2c and Figure S2).

To determine the absolute number of NPs that accumulated in the tumor, the %ID/g plots were transformed to number of NPs/g of tissue by considering the surface covered by an individual lipid (0.64, 0.25, and 0.72 nm[2] for DSPC, cholesterol, and PEG$_{2000}$-DSPE, respectively), their molar ratio in the final recipe (62, 33, 5% for DSPC, cholesterol, and PEG$_{2000}$-DSPE respectively), and the radius of the different NPs (50 and 75 nm for liposomes and nanoemulsions). Based on these, the total number of lipids per NP (121 and 137 K lipids per liposome and nanoemulsion respectively), the total injected amount (80 μmol lipid per kg), and the absolute number of NPs reaching the tumor at the various time points were calculated (Figure S3).

PET/CT Acquisition and Reconstruction. All 80 mice used for pharmacokinetic and biodistribution profile determinations underwent PET/CT at 1, 2, 4, and 12/24 h (n = 5 per NP per time point, totaling 80 scans). Before the scan, mice were anesthetized with isoflurane (Baxter Healthcare, Deerfield, IL)/oxygen gas mixture (2% for induction, 1% for maintenance), and subsequently imaged on a Mediso nanoScan PET/CT scanner (Mediso, Budapest, Hungary). The PET acquisition time for all scans was 20 min. Prior to the PET acquisition, a 3 min whole-body CT scan was performed (energy 50 kVp, current 180 μAs, isotropic voxel size at 0.25 × 0.25 mm). The coincidences were filtered with an energy window between 400 and 600 keV. The voxel size was isotropic with 0.6 mm width, and the reconstruction was applied for two full iterations, six subsets per iteration. PET data were reconstructed using CT-based attenuation correction. Reconstruction was performed using the TeraTomo 3D reconstruction algorithm from the Mediso Nucline software. Immediately after the PET/CT scan, animals were euthanized.

PET/CT Analysis. For NP biodistribution comparisons (Figure 2a,b and Figure S4a) for each scanned animal 11−12 ROIs for liver and tumor, 6−7 ROIs for spleen and heart covering the whole organ on a 2−3 slices step were averaged. For NP spatial distribution in the tumor (Figure 2d−f and Figure S4d,e), whole tumors and tumor cores (defined as the volumes at half the tumor diameter, resulting in approximately 20% of total tumor volume) were defined to obtain the standardized uptake value (SUV) in corresponding volumes. For ROI designing and activity quantification OsiriX MD software was used.

For PET/CT image presentation, 3D Slicer software and InVesalius software were used. For the 3D reconstructions of animals injected with cRGD-NPs (Figure 1), the scanning bed was masked out from the CT images, after which 3D renderings of the skeletal bones were produced. These were overlaid with 3D renderings of the tumor and biodistribution of the NPs as visualized by PET. For the biodistribution images (Figure 2a and Figure S4a), the CT images were window-leveled from −1000 to 2000 HU and the PET images were window-leveled from 0 to 1.25 for nanoemulsions (Figure 2a) or 0 to 3 MBq/mL for liposomes (Figure S4a). Finally, the CT images were overlain with their

corresponding PET images at 50% opacity. For presentation of NP distribution through the tumors (Figure 2d and Figure S4d), the tumor was manually delineated in a single coronal slice approximately through the middle of the tumor. The intensity of the PET images was window-leveled from 0 to 100 for nano-emulsions and from 0 to 250 kBq/mL for liposomes.

Intravital Microscopy. In all IVM experiments, mice were anesthetized (subcutaneous injection of a mixture of fentanyl (0.05 mg/kg), medetomidine (0.5 mg/kg), midazolam (0.5 mg/kg), and water (2:1:2:5) at a dose of 0.1 mL per 10 g of body weight) and cannulated in the tail vein. Window chamber mice were fixed on a custom heated microscope stage. Directly after intravenous administration of a NP bolus (80 μmol lipid per kg, n = 3−5 per NP), laser power and detector gain were adjusted, and from 1 to 2 min post-injection, animals were imaged dynamically (temporal resolution of 30 s) for at least 30 min. To study uptake in circulating cells, we employed high-speed imaging with temporal resolution of 0.3−2 s at various time points post-injection. Static images and z-stacks were obtained at various time points up to 24 h post-injection as well. To study differences between cRGD- and cRAD-formulations *in vivo*, we co-injected mice with cRGD- and cRAD-NPs labeled with ATTO633-PE and rhodamine-PE, respectively (40 μmol lipid per kg for each formulation, n = 2 for both NE and liposomes). For IVM on orthotopic tumors, an incision around 70% of the tumor was made. The skin and tumor were carefully detached from the mouse such that a 'skinflap' with the tumor on it was obtained. Using an operating microscope, the fat tissue surrounding the tumor was carefully removed, without damaging blood vessels. Subsequently, the tumor was submerged in a small 'bath' of PBS (contained in a rubber ring glued to a coverglass) with the skin side facing upward. The tumor was fixed using a second rubber ring and tape. For IVM on healthy ear tissue, the mice (n = 2 per NP combination) were placed in a supine position, and the ear was placed on a 0.17 mm microscope glass slide and embedded in glycerine. A cover glass was carefully taped on top of each ear to level the skin on the glass slide. Care was taken to allow blood flow through the ear after fixation. The cover glass was stabilized with tape. Finally, the mice were placed on a heated microscope stage, injected with NPs (n = 2 per NP), and imaged up to 3 h post-injection. IVM was performed on a confocal laser scanning microscope (Leica SP8) using a 20×/0.5 air objective in case of window chambers and a 25×/1.95 water immersion objective in case of orthotopic tumor imaging. This system is equipped with a tunable white light laser as well as a tunable bandpass detection system. Brilliant Violet 421-CD45-antibody (4 μg, intravenously injected to stain circulating immune cells) was excited with 405 nm and detected at 420−470 nm. GFP and Alexa Fluor 488-Dextran (2 MDa, intravenously injected to delineate circulating cells that do not take up dextran) were both excited at 488 nm, but detected at 500−515 nm and 500−550 nm, respectively. ATTO633 was excited at 633 nm and detected at 645−700 nm, and rhodamine was excited at 560 nm and detected at 570−600 nm. Obtained images and image stacks were analyzed and prepared for publication using ImageJ, and graphs were plotted with Matlab.

Ex Vivo Microscopy. To study NP uptake in circulating cells with *ex vivo* confocal laser scanning microscopy (CLSM), we co-injected cRGD- and cRAD-NPs labeled with ATTO633-PE and rhodamine-PE, respectively (40 μmol lipid per kg for each formulation). To ensure fluorescent labeling did not affect our read-out, we also co-injected oppositely labeled formulations. We collected 0.5−1 mL of blood *via* a heart puncture at 5 or 10 min or 2 h post-injection in 1 mL of 1 IU/mL heparin in 0.9% NaCl. White cells were isolated using Lymphoprep (Nycomed Pharma) according to the manufacturer's instructions, concentrated using centrifugation, transferred to ibidi wells, and imaged directly with the Leica SP8 using the same laser and detector configurations as during IVM. Images and z-stacks were acquired using a 40×/1.1 water objective. Figure S5 reports the results for *ex vivo* CLSM on isolated white cells.

Flow Cytometry. For flow cytometrical analysis, mice bearing 66cl4 orthotopic tumors were injected with NPs (80 μmol lipid per

kg, n = 3−6 per NP per time point). At 4, 12, and 24 h post-injection mice were sacrificed, and approximately 1 mL of blood was collected from the heart and placed in 15 mL tube containing 1 mL of heparin 1 IU in 0.9% NaCl. Then, mice were perfused with PBS (10−15 mL) until all blood was visibly perfused out of liver and kidneys. Tumors were resected, weighted, and placed in serum-free RPMI on ice until ready to mince and digest. To prepare blood samples for flow cytometry, red cell lysis buffer (1 part 0.17N Tris (pH = 7.65) mixed with 50 parts 0.16N NH4Cl, final pH = 7.2) was made fresh, and red cells were lysed (1:5 blood volume/lysis buffer volume) at room temperature for 5 min. The tube with blood and lysis buffer was filled with serum-free RPMI, and the suspension was centrifuged at 340 g for 8 min at 4 °C. The supernatant was aspirated out, and the lysis process was repeated once. The obtained immune cell pellet was resuspended in 500 μL of FACS buffer (PBS, supplemented with 2% fetal calf serum and 2 mM EDTA) and incubated with 5.0 μg of TruStain fcX (antimouse CD16/32) antibody for 10 min on ice.

To obtain tumor single cell suspensions, tumors were minced to 0.5 mm pieces in an uncoated Petri dish containing 2 mL of serum-free RPMI using a scalpel. The minced tumor was placed in a tube containing 4 mL of enzyme solution (120 μL Liberase DL (0.835 U/mL), 240 μL Liberase TL (0.835 U/mL), and 40 μL DNase I (13 U/mL) and incubated for 30 min at 37 °C on a shaking incubator. Then, the sample was filtered through a 70 μm filter. Tumor pieces not able to go through the filter were further ground using a syringe plunger. The tumor single-cell suspension was washed with serum-free RPMI, and one red cell lysis step was performed. The cells were suspended in 500 μL of FACS buffer and incubated with 5.0 μg of TruStain fcX (antimouse CD16/32) antibody for 10 min on ice. 100 μL of blood and tumor samples were incubated for 30 min on ice with fluorescent antibodies, as described in Table S2.

Right before the flow cytometry run, each sample was supplemented with one test of 7-AAD live/dead marker (A1310, ThermoFisher Scientific). For compensating fluorophore detection, single color samples were run under the same laser voltage conditions. The flow cytometry data were analyzed using Kaluza software. Cellular fragments and debris were gated out of the analysis by utilizing forward and side angle light scatter signal. As a negative control for determination of NP uptake, blood and tumor single cell suspensions from non-injected mice were used. Panel 1 was used to determine immune cell α_v and β_3 integrin subunit expression (Figure 5a and Figure S11). Panels 2−4 (for which the gating strategy is presented in Figure S7) were utilized for studying the cRGD- and cRAD-NP uptake by circulating immune cells (Figures S8a,b and S9a), tumor associated immune cells (Figures S8c,d and S9b), and tumor endothelial cells (Figure S12). The antibodies were purchased from Biolegend (Brilliant Violet 421-CD11b, clone M1/70, 101235; Brilliant Violet 421-CD45, clone 30-F11, 103133; Brilliant Violet 510-Ly6G, clone 1A8, 127633; Alexa Fluor 488-CD61, clone 2C9.G2, 104311; Alexa Fluor 488-CD103, clone 2E7, 121408; PE-CD51, clone RMV-7, 104105; PE-F4/80, clone BM8, 123110; PE/Cy7-CD19, clone 6D5, 115520; PE/Cy7-NK-1.1, clone PK136, 108714; PE/Cy7-CD31, clone MEC13.3, 102524; Alexa Fluor 700-CD11c, clone N418, 117320; Alexa Fluor 700-CD45, clone 30-F11, 103128; APC-Fire750-Ly6C, clone HK1.4, 128046; APC-Fire750-CD31, clone MEC13.3, 102528) or ThermoFisher (APC-eFluor780-CD3e, clone HK1.4, 128046) (Table S3). To evaluate NP uptake and determine percent positive cells, we set the border between negative and positive cells such that the negative control cells were <2% positive. For the reported X_{median} values, the following calculation was conducted:

$$X_{\text{median reported}} = X_{\text{median of cells from mice injected with nanoparticles}}$$
$$- X_{\text{median of cells from non-injected mice}}$$

Histology. For histological analysis of tumors, 18 BALB/c mice were inoculated orthotopically with 5×10^6 66cl4 cells. 14−21 days post-inoculation, mice were sacrificed and perfused with 10−15 mL PBS. Tumors were collected and embedded with OCT compound

and snap frozen in 2-methylbutane (M32631, Sigma-Aldrich Inc.) 2-Methylbutane was cooled down to −20 °C in dry ice for approximately 1 min. The samples were placed on −80 °C overnight. Next, the tissue was cut in a cryostat at 8 μm in consecutive sections.

For histological staining, sections were fixed in 95% ethyl alcohol for 15 s. Samples were then dipped 10 times into formalin 10%, (phosphate buffered, SF100-4 10% buffered formalin phosphate, Fisher Scientific) and rinsed in water (10 dips). Slides were stained with hematoxylin stain (Part 1201A hematoxylin stain, Harris Modified, Newcomer Supply) for 30 s and washed in two changes of distilled water for 10 dips, followed by 95% ethyl alcohol for 10 dips. The counterstaining was done in eosin Y working solution (Part 1072A eosin Y working solution, Newcomer Supply) for 15 s, and the sections were subsequently dehydrated in two changes of 95% ethyl alcohol and two changes of 100% ethyl alcohol (UN1170 ethanol 200 proof Anhydrous, Decon Laboratories) (10 dips each). Slides were then cleared in two changes of xylene (10 dips each). The coverslip was done in cytoseal XYL (8312-4 Cytoseal XYL, Richard-Allan Scientific). For imaging hematoxylin and eosin (H&E) stained slices, a Zeiss Axio Imager Z2M with a 10×/0.3 air and a 20×/0.8 air objective were used (Figure S 4d).

For immunofluorescence staining, tumor slices neighboring the H&E stained sections were fixed in −20 °C acetone for 10 min and washed twice with PBS for 5 min. The slices were blocked with TBS buffer (37581 SuperBlock Blocking Buffer, Life Technologies) for 20 min at room temperature in a humid chamber. After the samples were washed with PBS, slides were incubated with 5 μg/mL Alexa Fluor 594 antimouse CD31 antibody (102432, Biolegend) in TBS buffer overnight at 4 °C. This was followed by three wash steps of 5 min each with PBS. Excess of liquid was removed and slides were mounted with VECTASHIELD Vibrance Antifade Mounting Medium with DAPI (H-1800-10, Vector laboratories). Fluorescence-labeled tumor slices were imaged using a Leica SP5 DMI confocal microscope equipped with 20×/0.7 air, 40×/1.25 oil, and 63×/1.4 oil objectives. DAPI and Alexa Fluor 594 were excited with a UV diode at 405 nm and a DPSS 561 nm laser and detected at 430−490 nm and 590−630 nm, respectively (Figure S4c). Both H&E and CD31 staining revealed an homogeneous physiology in the 66cl4 tumors, the absence of a necrotic core, and homogeneous tumor vascularization (Figure S4b,c).

Statistical Analysis. All data are presented as mean ± standard error of the mean (SEM), unless otherwise indicated. Flow cytometry data were tested for significance using a two-tailed unpaired t test for comparing two groups in GraphPad Prism version 8.0.2 software. P-values < 0.05 were considered significant, with levels of significance being indicated as follows: * $p < 0.05$; ** $p < 0.01$; *** $p < 0.001$; **** $p < 0.0001$; ns, not significant. Number of animals per experiment is indicated in the figure legends. An overview of the total number of animals used in each experimental procedure is provided in Figure S14.

ASSOCIATED CONTENT

Ⓢ Supporting Information

The Supporting Information is available free of charge at https://pubs.acs.org/doi/10.1021/acsnano.9b08693.

Figure S1: Nanoparticle characterization and pharmacokinetic profile. Figure S2: Nanoparticle biodistribution profile. Figure S3: Nanoparticle distribution in the tumor tissue over time. Figure S4: PET/CT of liposome injected animals and histological analysis of 66cl4 tumors. Figure S5: *Ex vivo* CLSM on white blood cells isolated at 5 or 10 min or 2 h post-injection. Figure S6: IVM images obtained in tumors growing in window chamber mice. Figure S7: Flow cytometry gating strategy on blood, tumor, and tumor endothelium. Figure S8: Flow cytometry histograms reveal nanoparticle uptake by circulating and tumor associated immune cells. Figure S9: Flow cytometry-based bar chart shows nanoparticle uptake by circulating and tumor associated immune cells. Figure S10: 66cl4 tumor cell profiling. Figure S11: Association of circulating immune cells with α_v and β_3 integrin subunits. Figure S12: Nanoparticle uptake by tumor endothelial cells as a function of α_v and β_3 integrin expression levels. Figure S13: cRGD-NP positive immune cells do not extravasate in healthy ear tissue. Figure S14: Number of mice used per experimental procedure. Table S1: Nanoparticle composition. Table S2: Flow cytometry panels. Table S3: Used antibodies (PDF)

Movies S1−S13: Movies obtained in tumors grown in dorsal window chambers showing extensive cRGD-nanoparticle uptake in circulating immune cells and hitchhiking of cRGD-liposomes and cRGD-nanoemulsions (and not of cRAD-nanoparticles) with cells from the vasculature into the tumor tissue. Movie S1: Immune cell uptake in the circulation for cRGD-nanoemulsions during the first hour post-injection (AVI)

Movie S2: Immune cell uptake in the circulation for cRGD-liposomes during the first hour post-injection (AVI)

Movie S3: Intravital CD45-staining confirmed the presence of bound and circulating cRGD-nanoparticle positive immune cells (AVI)

Movie S4: cRAD-nanoemulsions were hardly taken up by immune cells during the first hour post-injection (AVI)

Movie S5: cRAD-liposomes were hardly taken up by immune cells during the first hour post-injection (AVI)

Movie S6: Significant immune cell uptake of circulating cRGD-nanoemulsions at later time points post-injection (AVI)

Movie S7: Significant immune cell uptake of circulating cRGD-liposomes at later time points post-injection (AVI)

Movie S8: cRAD-nanoemulsions were taken-up by circulating cells, but to much lower extent (AVI)

Movie S9: cRAD-liposomes were taken-up by circulating cells, but to much lower extent (AVI)

Movie S10: cRAD- and cRGD-nanoemulsions co-injections corroborated that cRGD-nanoemulsions were taken up to higher extents than cRAD-nanoemulsions by circulating cells (AVI)

Movie S11: cRAD- and cRGD-liposomes co-injections corroborated that cRGD-liposomes were taken up to higher extents than cRAD-liposomes by circulating cells (AVI)

Movie S12: In tumors grown in window chamber mice we observed cRGD-nanoemulsions hitchhiking with immune cells from the circulation into the tumor tissue (AVI)

Movie S13: In tumors grown in window chamber mice we observed cRGD-liposomes hitchhiking with immune cells from the circulation into the tumor tissue (AVI)

Movies 14−17: Movies obtained in tumors grown orthotopically showing that cRGD-nanomaterial hitchhikes with cells into the tumor tissue where these cells display high motility. Hardly any accumulation of cRGD-nanoparticles in TAMs was observed. Movie

S14: cRGD-nanoparticle hitchhiking (nanoemulsion) (AVI)

Movie S15: cRGD-nanoparticles hardly accumulated in dextran positive TAMs up to 3 hours post-injection, but rather presented in mobile cells in the tumor tissue (liposomes) (AVI)

Movie S16: cRGD-nanoparticles hardly accumulated in dextran positive TAMs up to 3 hours post-injection, but rather presented in mobile cells in the tumor adjacent fat tissue (liposomes) (AVI)

Movie S17: Hardly any cRAD-nanoparticle hitchhiking was observed (nanoemulsion) (AVI)

Movies 18−19: Movies obtained in healthy ear tissue showing the same nanoparticle uptake patterns in healthy mice as in the tumor bearing animals and the absence of nanoparticle hitchhiking with cells into healthy tissue. Movie S18: cRGD-liposomes (24 h post-injection) injected in non-tumor bearing mice showed an extensive uptake by circulating immune cells in comparison to limited uptake of the control cRAD-liposomes by these cells (AVI)

Movie S19: cRGD-nanoemulsions (2 h post-injection) injected in non-tumor bearing mice showed an extensive uptake by circulating immune cells in comparison to limited uptake of the control cRAD-nanoemulsions by these cells (AVI)

AUTHOR INFORMATION

Corresponding Authors

Alexandros Marios Sofias − *Department of Circulation and Medical Imaging, Faculty of Medicine and Health Sciences, Norwegian University of Science and Technology (NTNU), 7030 Trondheim, Norway; BioMedical Engineering and Imaging Institute, Icahn School of Medicine at Mount Sinai, New York, New York 10029, United States; Department of Nanomedicine and Theranostics, Institute for Experimental Molecular Imaging, Faculty of Medicine, RWTH Aachen University, 52074 Aachen, Germany;* orcid.org/0000-0002-7475-2526; Email: alexandrosofias@outlook.com, asofias@ukaachen.de

Sjoerd Hak − *Department of Circulation and Medical Imaging, Faculty of Medicine and Health Sciences, Norwegian University of Science and Technology (NTNU), 7030 Trondheim, Norway; Department of Biotechnology and Nanomedicine, SINTEF Industry, 7034 Trondheim, Norway;* Email: sjoerd.hak@ntnu.no, sjoerd.hak@sintef.no

Authors

Yohana C. Toner − *BioMedical Engineering and Imaging Institute, Icahn School of Medicine at Mount Sinai, New York, New York 10029, United States*

Anu E. Meerwaldt − *BioMedical Engineering and Imaging Institute, Icahn School of Medicine at Mount Sinai, New York, New York 10029, United States; Biomedical MR Imaging and Spectroscopy Group, Center for Image Sciences, University Medical Center Utrecht and Utrecht University, 3584 CX Utrecht, The Netherlands*

Mandy M. T. van Leent − *BioMedical Engineering and Imaging Institute, Icahn School of Medicine at Mount Sinai, New York, New York 10029, United States; Department of Medical Biochemistry, Amsterdam University Medical Centers, 1105 AZ Amsterdam, The Netherlands*

Georgios Soultanidis − *BioMedical Engineering and Imaging Institute, Icahn School of Medicine at Mount Sinai, New York, New York 10029, United States*

Mattijs Elschot − *Department of Circulation and Medical Imaging, Faculty of Medicine and Health Sciences, Norwegian University of Science and Technology (NTNU), 7030 Trondheim, Norway; Department of Radiology and Nuclear Medicine, St. Olavs Hospital, Trondheim University Hospital, 7030 Trondheim, Norway*

Haruki Gonai − *BioMedical Engineering and Imaging Institute, Icahn School of Medicine at Mount Sinai, New York, New York 10029, United States*

Kristin Grendstad − *Department of Physics, Faculty of Natural Sciences, Norwegian University of Science and Technology (NTNU), 7034 Trondheim, Norway*

Åsmund Flobak − *The Cancer Clinic, St. Olav's University Hospital, 7030 Trondheim, Norway; Department of Clinical and Molecular Medicine, Faculty of Medicine and Health Sciences, Norwegian University of Science and Technology (NTNU), 7030 Trondheim, Norway*

Ulrike Neckmann − *Department of Biomedical Laboratory Science, Faculty of Natural Sciences and Centre of Molecular Inflammation Research (CEMIR), Faculty of Medicine and Health Sciences, Norwegian University of Science and Technology (NTNU), 7030 Trondheim, Norway*

Camilla Wolowczyk − *Department of Biomedical Laboratory Science, Faculty of Natural Sciences and Centre of Molecular Inflammation Research (CEMIR), Faculty of Medicine and Health Sciences, Norwegian University of Science and Technology (NTNU), 7030 Trondheim, Norway*

Elizabeth L. Fisher − *BioMedical Engineering and Imaging Institute, Icahn School of Medicine at Mount Sinai, New York, New York 10029, United States*

Thomas Reiner − *Department of Radiology, Memorial Sloan Kettering Cancer Center, New York, New York 10065, United States; Department of Radiology, Weill Cornell Medical College, New York, New York 10065, United States;* orcid.org/0000-0002-7819-5480

Catharina de Lange Davies − *Department of Physics, Faculty of Natural Sciences, Norwegian University of Science and Technology (NTNU), 7034 Trondheim, Norway*

Geir Bjørkøy − *Department of Clinical and Molecular Medicine, Faculty of Medicine and Health Sciences, Department of Biomedical Laboratory Science, Faculty of Natural Sciences, and Centre of Molecular Inflammation Research (CEMIR), Faculty of Medicine and Health Sciences, Norwegian University of Science and Technology (NTNU), 7030 Trondheim, Norway*

Abraham J. P. Teunissen − *BioMedical Engineering and Imaging Institute, Icahn School of Medicine at Mount Sinai, New York, New York 10029, United States;* orcid.org/0000-0002-0401-8262

Jordi Ochando − *Department of Oncological Sciences, Icahn School of Medicine at Mount Sinai, New York, New York 10029, United States; Transplant Immunology Unit, National Center of Microbiology, Instituto de Salud Carlos III, 28220 Madrid, Spain*

Carlos Pérez-Medina − *BioMedical Engineering and Imaging Institute, Icahn School of Medicine at Mount Sinai, New York, New York 10029, United States; Centro Nacional de Investigaciones Cardiovasculares Carlos III (CNIC), 28029 Madrid, Spain*

Willem J. M. Mulder − *BioMedical Engineering and Imaging Institute, Icahn School of Medicine at Mount Sinai, New York, New York 10029, United States; Department of Medical Biochemistry, Amsterdam University Medical Centers, 1105 AZ Amsterdam, The Netherlands; Laboratory of Chemical Biology, Department of Biochemical Engineering, Eindhoven University of Technology, 5612 AP Eindhoven, The Netherlands;* ⓞ orcid.org/0000-0001-8665-3878

Complete contact information is available at:
https://pubs.acs.org/10.1021/acsnano.9b08693

Author Contributions

S.H. and W.J.M.M. conceptualized the study. A.M.S., C.P.M., W.J.M.M., and S.H. designed the study. A.M.S. and S.H. planned the experiments and A.M.S. coordinated their execution. Nanoparticles were synthesized and characterized by A.M.S. and S.H. and radiolabeled by A.J.P.T., T.R., and C.P.M. Gamma counting experiments were conducted by A.M.S., Y.C.T., A.E.M., and M.M.T.vL. PET/CT imaging and analysis was conducted by A.M.S., G.S., M.E., H.G., and E.L.F. IVM and *ex vivo* microscopy was conducted by A.M.S. and S.H. Dorsal window chambers were implanted by K.G. Flow cytometry experiments and data analysis were conducted by A.M.S. Flow cytometry protocols were developed by A.M.S., U.N., C.W., and S.H. Immunological insights were provided by G.B. and J.O. Histology experiments and analysis were conducted by A.M.S. and Y.C.T. S.H. and A.M.S. wrote the manuscript and produced the figures. All authors contributed to data interpretation and reviewed, edited, and approved the manuscript before submission.

Notes

The authors declare the following competing financial interest(s): J.O. and W.J.M.M. are scientific founders of Trained Therapeutix Discovery.

REFERENCES

(1) Barenholz, Y. Doxil® — The First FDA-Approved Nano-Drug: Lessons Learned. *J. Controlled Release* **2012**, *160*, 117−134.

(2) van der Meel, R.; Vehmeijer, L. J. C.; Kok, R. J.; Storm, G.; van Gaal, E. V. B. Ligand-Targeted Particulate Nanomedicines Undergoing Clinical Evaluation: Current Status. *Adv. Drug Delivery Rev.* **2013**, *65*, 1284−1298.

(3) Witzigmann, D.; Hak, S.; van der Meel, R. Translating Nanomedicines: Thinking beyond Materials? A Young Investigator's Reply to 'The Novelty Bubble.'. *J. Controlled Release* **2018**, *290*, 138−140.

(4) Hua, S.; de Matos, M. B. C.; Metselaar, J. M.; Storm, G. Current Trends and Challenges in the Clinical Translation of Nanoparticulate Nanomedicines: Pathways for Translational Development and Commercialization. *Front. Pharmacol.* **2018**, *9*, 790.

(5) Chu, D.; Zhao, Q.; Yu, J.; Zhang, F.; Zhang, H.; Wang, Z. Nanoparticle Targeting of Neutrophils for Improved Cancer Immunotherapy. *Adv. Healthcare Mater.* **2016**, *5*, 1088−1093.

(6) Miller, M. A.; Zheng, Y.-R.; Gadde, S.; Pfirschke, C.; Zope, H.; Engblom, C.; Kohler, R. H.; Iwamoto, Y.; Yang, K. S.; Askevold, B.; Kolishetti, N.; Pittet, M.; Lippard, S. J.; Farokhzad, O. C.; Weissleder, R. Tumour-Associated Macrophages Act as a Slow-Release Reservoir of Nano-Therapeutic Pt(IV) Pro-Drug. *Nat. Commun.* **2015**, *6*, 8692.

(7) Tang, J.; Baxter, S.; Menon, A.; Alaarg, A.; Sanchez-Gaytan, B. L.; Fay, F.; Zhao, Y.; Ouimet, M.; Braza, M. S.; Longo, V. A.; Abdel-Atti, D.; Duivenvoorden, R.; Calcagno, C.; Storm, G.; Tsimikas, S.; Moore, K. J.; Swirski, F. K.; Nahrendorf, M.; Fisher, E. A.; Pérez-Medina, C.; et al. Immune Cell Screening of a Nanoparticle Library Improves Atherosclerosis Therapy. *Proc. Natl. Acad. Sci. U. S. A.* **2016**, *113*, E6731−E6740.

(8) Duro-Castano, A.; Gallon, E.; Decker, C.; Vicent, M. J. Modulating Angiogenesis with Integrin-Targeted Nanomedicines. *Adv. Drug Delivery Rev.* **2017**, *119*, 101−119.

(9) Wu, P.-H.; Onodera, Y.; Ichikawa, Y.; Rankin, E.; Giaccia, A.; Watanabe, Y.; Qian, W.; Hashimoto, T.; Shirato, H.; Nam, J.-M. Targeting Integrins with RGD-Conjugated Gold Nanoparticles in Radiotherapy Decreases the Invasive Activity of Breast Cancer Cells. *Int. J. Nanomed.* **2017**, *12*, 5069−5085.

(10) Ng, Q. K. T.; Olariu, C. I.; Yaffee, M.; Taelman, V. F.; Marincek, N.; Krause, T.; Meier, L.; Walter, M. A. Indium-111 Labeled Gold Nanoparticles for *In Vivo* Molecular Targeting. *Biomaterials* **2014**, *35*, 7050−7057.

(11) Zhan, C.; Gu, B.; Xie, C.; Li, J.; Liu, Y.; Lu, W. Cyclic RGD Conjugated Poly(Ethylene Glycol)-Co-Poly(Lactic Acid) Micelle Enhances Paclitaxel Anti-Glioblastoma Effect. *J. Controlled Release* **2010**, *143*, 136−142.

(12) Huang, Y.; Liu, W.; Gao, F.; Fang, X.; Chen, Y. C(RGDyK)-Decorated Pluronic Micelles for Enhanced Doxorubicin and Paclitaxel Delivery to Brain Glioma. *Int. J. Nanomed.* **2016**, *11*, 1629.

(13) Schiffelers, R. M.; Koning, G. A.; ten Hagen, T. L.; Fens, M. H. A.; Schraa, A. J.; Janssen, A. P. C.; Kok, R. J.; Molema, G.; Storm, G. Anti-Tumor Efficacy of Tumor Vasculature-Targeted Liposomal Doxorubicin. *J. Controlled Release* **2003**, *91*, 115−122.

(14) Miura, Y.; Takenaka, T.; Toh, K.; Wu, S.; Nishihara, H.; Kano, M. R.; Ino, Y.; Nomoto, T.; Matsumoto, Y.; Koyama, H.; Cabral, H.; Nishiyama, N.; Kataoka, K. Cyclic RGD-Linked Polymeric Micelles for Targeted Delivery of Platinum Anticancer Drugs to Glioblastoma through the Blood-Brain Tumor Barrier. *ACS Nano* **2013**, *7*, 8583−8592.

(15) Anselmo, A. C.; Mitragotri, S. Nanoparticles in the Clinic: An Update. *Bioeng. Transl. Med.* **2019**, *4*, e10143.

(16) Sofias, A. M.; Dunne, M.; Storm, G.; Allen, C. The Battle of "Nano" Paclitaxel. *Adv. Drug Delivery Rev.* **2017**, *122*, 20−30.

(17) Pattni, B. S.; Chupin, V. V.; Torchilin, V. P. New Developments in Liposomal Drug Delivery. *Chem. Rev.* **2015**, *115*, 10938−10966.

(18) Hörmann, K.; Zimmer, A. Drug Delivery and Drug Targeting with Parenteral Lipid Nanoemulsions — A Review. *J. Controlled Release* **2016**, *223*, 85−98.

(19) Pérez-Medina, C.; Abdel-Atti, D.; Tang, J.; Zhao, Y.; Fayad, Z. A.; Lewis, J. S.; Mulder, W. J. M.; Reiner, T. Nanoreporter PET Predicts the Efficacy of Anti-Cancer Nanotherapy. *Nat. Commun.* **2016**, *7*, 11838.

(20) Danhier, F.; Le Breton, A.; Préat, V. RGD-Based Strategies To Target Alpha(v) Beta(3) Integrin in Cancer Therapy and Diagnosis. *Mol. Pharmaceutics* **2012**, *9*, 2961−2973.

(21) Schiffelers, R. M.; Ansari, A.; Xu, J.; Zhou, Q.; Tang, Q.; Storm, G.; Molema, G.; Lu, P. Y.; Scaria, P. V.; Woodle, M. C. Cancer SiRNA Therapy by Tumor Selective Delivery with Ligand-Targeted Sterically Stabilized Nanoparticle. *Nucleic Acids Res.* **2004**, *32*, No. e149.

(22) Fan, Z.; Chang, Y.; Cui, C.; Sun, L.; Wang, D. H.; Pan, Z.; Zhang, M. Near Infrared Fluorescent Peptide Nanoparticles for Enhancing Esophageal Cancer Therapeutic Efficacy. *Nat. Commun.* **2018**, *9*, 2605.

(23) Yang, K.; Liu, Y.; Liu, Y.; Zhang, Q.; Kong, C.; Yi, C.; Zhou, Z.; Wang, Z.; Zhang, G.; Zhang, Y.; Khashab, N. M.; Chen, X.; Nie,

Z. Cooperative Assembly of Magneto-Nanovesicles with Tunable Wall Thickness and Permeability for MRI-Guided Drug Delivery. *J. Am. Chem. Soc.* **2018**, *140*, 4666−4677.

(24) Yu, G.; Yang, Z.; Fu, X.; Yung, B. C.; Yang, J.; Mao, Z.; Shao, L.; Hua, B.; Liu, Y.; Zhang, F.; Fan, Q.; Wang, S.; Jacobson, O.; Jin, A.; Gao, C.; Tang, X.; Huang, F.; Chen, X. Polyrotaxane-Based Supramolecular Theranostics. *Nat. Commun.* **2018**, *9*, 766.

(25) Kimball, K. J.; Preuss, M. A.; Barnes, M. N.; Wang, M.; Siegal, G. P.; Wan, W.; Kuo, H.; Saddekni, S.; Stockard, C. R.; Grizzle, W. E.; Harris, R. D.; Aurigemma, R.; Curiel, D. T.; Alvarez, R. D. A Phase I Study of a Tropism-Modified Conditionally Replicative Adenovirus for Recurrent Malignant Gynecologic Diseases. *Clin. Cancer Res.* **2010**, *16*, 5277−5287.

(26) Pesonen, S.; Diaconu, I.; Cerullo, V.; Escutenaire, S.; Raki, M.; Kangasniemi, L.; Nokisalmi, P.; Dotti, G.; Guse, K.; Laasonen, L.; Partanen, K.; Karli, E.; Haavisto, E.; Oksanen, M.; Karioja-Kallio, A.; Hannuksela, P.; Holm, S.-L.; Kauppinen, S.; Joensuu, T.; Kanerva, A.; et al. Integrin Targeted Oncolytic Adenoviruses Ad5-D24-RGD and Ad5-RGD-D24-GMCSF for Treatment of Patients with Advanced Chemotherapy Refractory Solid Tumors. *Int. J. Cancer* **2012**, *130*, 1937−1947.

(27) Phillips, E.; Penate-Medina, O.; Zanzonico, P. B.; Carvajal, R. D.; Mohan, P.; Ye, Y.; Humm, J.; Gönen, M.; Kalaigian, H.; Schöder, H.; Strauss, H. W.; Larson, S. M.; Wiesner, U.; Bradbury, M. S. Clinical Translation of an Ultrasmall Inorganic Optical-PET Imaging Nanoparticle Probe. *Sci. Transl. Med.* **2014**, *6*, 260ra149.

(28) Dubey, P. K.; Mishra, V.; Jain, S.; Mahor, S.; Vyas, S. P. Liposomes Modified with Cyclic RGD Peptide for Tumor Targeting. *J. Drug Target.* **2004**, *12*, 257−264.

(29) Mulder, W. J. M.; van der Schaft, D. W. J.; Hautvast, P. A. I.; Strijkers, G. J.; Koning, G. A.; Storm, G.; Mayo, K. H.; Griffioen, A. W.; Nicolay, K. Early *In Vivo* Assessment of Angiostatic Therapy Efficacy by Molecular MRI. *FASEB J.* **2007**, *21*, 378−383.

(30) Hak, S.; Cebulla, J.; Huuse, E. M.; Davies, C. d. L.; Mulder, W. J. M.; Larsson, H. B. W.; Haraldseth, O. Periodicity in Tumor Vasculature Targeting Kinetics of Ligand-Functionalized Nanoparticles Studied by Dynamic Contrast Enhanced Magnetic Resonance Imaging and Intravital Microscopy. *Angiogenesis* **2014**, *17*, 93−107.

(31) Mulder, W. J. M.; Castermans, K.; van Beijnum, J. R.; oude Egbrink, M. G. A.; Chin, P. T. K.; Fayad, Z. A.; Löwik, C. W. G. M.; Kaijzel, E. L.; Que, I.; Storm, G.; Strijkers, G. J.; Griffioen, A. W.; Nicolay, K. Molecular Imaging of Tumor Angiogenesis Using Avβ3-Integrin Targeted Multimodal Quantum Dots. *Angiogenesis* **2009**, *12*, 17−24.

(32) Sofias, A. M.; Åslund, A. K. O.; Hagen, N.; Grendstad, K.; Hak, S. Simple and Robust Intravital Microscopy Procedures in Hybrid TIE2GFP-BALB/c Transgenic Mice. *Mol. Imaging Biol.* **2019**, 1−8.

(33) DeNardo, D. G.; Ruffell, B. Macrophages as Regulators of Tumour Immunity and Immunotherapy. *Nat. Rev. Immunol.* **2019**, *19*, 369−382.

(34) Coffelt, S. B.; Wellenstein, M. D.; de Visser, K. E. Neutrophils in Cancer: Neutral No More. *Nat. Rev. Cancer* **2016**, *16*, 431−446.

(35) Moses, K.; Brandau, S. Human Neutrophils: Their Role in Cancer and Relation to Myeloid-Derived Suppressor Cells. *Semin. Immunol.* **2016**, *28*, 187−196.

(36) Barros-Becker, F.; Lam, P.-Y.; Fisher, R.; Huttenlocher, A. Live Imaging Reveals Distinct Modes of Neutrophil and Macrophage Migration within Interstitial Tissues. *J. Cell Sci.* **2017**, *130*, 3801−3808.

(37) Sofias, A. M.; Andreassen, T.; Hak, S. Nanoparticle Ligand-Decoration Procedures Affect *In Vivo* Interactions with Immune Cells. *Mol. Pharmaceutics* **2018**, *15*, 5754−5761.

(38) Summers, C.; Rankin, S. M.; Condliffe, A. M.; Singh, N.; Peters, A. M.; Chilvers, E. R. Neutrophil Kinetics in Health and Disease. *Trends Immunol.* **2010**, *31*, 318−324.

(39) Colditz, I. G. Margination and Emigration of Leucocytes. *Pathol. Immunopathol. Res.* **1985**, *4*, 44−68.

(40) Hak, S.; Helgesen, E.; Hektoen, H. H.; Huuse, E. M.; Jarzyna, P. A.; Mulder, W. J. M.; Haraldseth, O.; Davies, C. de L. The Effect of Nanoparticle Polyethylene Glycol Surface Density on Ligand-Directed Tumor Targeting Studied *In Vivo* by Dual Modality Imaging. *ACS Nano* **2012**, *6*, 5648−5658.

(41) Smith, B. R.; Cheng, Z.; De, A.; Koh, A. L.; Sinclair, R.; Gambhir, S. S. Real-Time Intravital Imaging of RGD-Quantum Dot Binding to Luminal Endothelium in Mouse Tumor Neovasculature. *Nano Lett.* **2008**, *8*, 2599−2606.

(42) Smith, B. R.; Cheng, Z.; De, A.; Rosenberg, J.; Gambhir, S. S. Dynamic Visualization of RGD-Quantum Dot Binding to Tumor Neovasculature and Extravasation in Multiple Living Mouse Models Using Intravital Microscopy. *Small* **2010**, *6*, 2222−2229.

(43) Danhier, F.; Vroman, B.; Lecouturier, N.; Crokart, N.; Pourcelle, V.; Freichels, H.; Jérôme, C.; Marchand-Brynaert, J.; Feron, O.; Préat, V. Targeting of Tumor Endothelium by RGD-Grafted PLGA-Nanoparticles Loaded with Paclitaxel. *J. Controlled Release* **2009**, *140*, 166−173.

(44) Amin, M.; Mansourian, M.; Koning, G. A.; Badiee, A.; Jaafari, M. R.; ten Hagen, T. L. M. Development of a Novel Cyclic RGD Peptide for Multiple Targeting Approaches of Liposomes to Tumor Region. *J. Controlled Release* **2015**, *220*, 308−315.

(45) Hou, J.; Yang, X.; Li, S.; Cheng, Z.; Wang, Y.; Zhao, J.; Zhang, C.; Li, Y.; Luo, M.; Ren, H.; Liang, J.; Wang, J.; Wang, J.; Qin, J. Accessing Neuroinflammation Sites: Monocyte/Neutrophil-Mediated Drug Delivery for Cerebral Ischemia. *Sci. Adv.* **2019**, *5*, No. eaau8301.

(46) Jain, S.; Mishra, V.; Singh, P.; Dubey, P.; Saraf, D.; Vyas, S. RGD-Anchored Magnetic Liposomes for Monocytes/Neutrophils-Mediated Brain Targeting. *Int. J. Pharm.* **2003**, *261*, 43−55.

(47) Kunjachan, S.; Pola, R.; Gremse, F.; Theek, B.; Ehling, J.; Moeckel, D.; Hermanns-Sachweh, B.; Pechar, M.; Ulbrich, K.; Hennink, W. E.; Storm, G.; Lederle, W.; Kiessling, F.; Lammers, T. Passive *versus* Active Tumor Targeting Using RGD- and NGR-Modified Polymeric Nanomedicines. *Nano Lett.* **2014**, *14*, 972−981.

(48) Kirpotin, D. B.; Drummond, D. C.; Shao, Y.; Shalaby, M. R.; Hong, K.; Nielsen, U. B.; Marks, J. D.; Benz, C. C.; Park, J. W. Antibody Targeting of Long-Circulating Lipidic Nanoparticles Does Not Increase Tumor Localization but Does Increase Internalization in Animal Models. *Cancer Res.* **2006**, *66*, 6732−6740.

(49) Dai, Q.; Wilhelm, S.; Ding, D.; Syed, A. M.; Sindhwani, S.; Zhang, Y.; Chen, Y. Y.; MacMillan, P.; Chan, W. C. W. Quantifying the Ligand-Coated Nanoparticle Delivery to Cancer Cells in Solid Tumors. *ACS Nano* **2018**, *12*, 8423−8435.

(50) Panneerselvam, S.; Choi, S. Nanoinformatics: Emerging Databases and Available Tools. *Int. J. Mol. Sci.* **2014**, *15*, 7158−7182.

(51) Liarski, V. M.; Sibley, A.; van Panhuys, N.; Ai, J.; Chang, A.; Kennedy, D.; Merolle, M.; Germain, R. N.; Giger, M. L.; Clark, M. R. Quantifying *In Situ* Adaptive Immune Cell Cognate Interactions in Humans. *Nat. Immunol.* **2019**, *20*, 503−513.

(52) Giger, M. L. Machine Learning in Medical Imaging. *J. Am. Coll. Radiol.* **2018**, *15*, 512−520.

(53) Kim, H. J.; Lee, S.-M.; Park, K.-H.; Mun, C. H.; Park, Y.-B.; Yoo, K.-H. Drug-Loaded Gold/Iron/Gold Plasmonic Nanoparticles for Magnetic Targeted Chemo-Photothermal Treatment of Rheumatoid Arthritis. *Biomaterials* **2015**, *61*, 95−102.

(54) Koning, G. A.; Schiffelers, R. M.; Wauben, M. H. M.; Kok, R. J.; Mastrobattista, E.; Molema, G.; ten Hagen, T. L. M.; Storm, G. Targeting of Angiogenic Endothelial Cells at Sites of Inflammation by Dexamethasone Phosphate-Containing RGD Peptide Liposomes Inhibits Experimental Arthritis. *Arthritis Rheum.* **2006**, *54*, 1198−1208.

(55) Rodell, C. B.; Arlauckas, S. P.; Cuccarese, M. F.; Garris, C. S.; Li, R.; Ahmed, M. S.; Kohler, R. H.; Pittet, M. J.; Weissleder, R. TLR7/8-Agonist-Loaded Nanoparticles Promote the Polarization of Tumour-Associated Macrophages to Enhance Cancer Immunotherapy. *Nat. Biomed. Eng.* **2018**, *2*, 578−588.

(56) Dong, R.; Gong, Y.; Meng, W.; Yuan, M.; Zhu, H.; Ying, M.; He, Q.; Cao, J.; Yang, B. The Involvement of M2Macrophage

Polarization Inhibition in Fenretinide-Mediated Chemopreventive Effects on Colon Cancer. *Cancer Lett.* **2017**, *388*, 43−53.

(57) Sipkins, D. A.; Cheresh, D. A.; Kazemi, M. R.; Nevin, L. M.; Bednarski, M. D.; Li, K. C. P. Detection of Tumor Angiogenesis *In Vivo* by Avβ3-Targeted Magnetic Resonance Imaging. *Nat. Med.* **1998**, *4*, 623−626.

(58) Melemenidis, S.; Jefferson, A.; Ruparelia, N.; Akhtar, A. M.; Xie, J.; Allen, D.; Hamilton, A.; Larkin, J. R.; Perez-Balderas, F.; Smart, S. C.; Muschel, R. J.; Chen, X.; Sibson, N. R.; Choudhury, R. P. Molecular Magnetic Resonance Imaging of Angiogenesis *In Vivo* Using Polyvalent Cyclic RGD-Iron Oxide Microparticle Conjugates. *Theranostics* **2015**, *5*, 515−529.

(59) Kitagawa, T.; Kosuge, H.; Uchida, M.; Iida, Y.; Dalman, R. L.; Douglas, T.; McConnell, M. V. RGD Targeting of Human Ferritin Iron Oxide Nanoparticles Enhances *In Vivo* MRI of Vascular Inflammation and Angiogenesis in Experimental Carotid Disease and Abdominal Aortic Aneurysm. *J. Magn. Reson. Imaging* **2017**, *45*, 1144−1153.

(60) Huang, W.-C.; Chen, S.-H.; Chiang, W.-H.; Huang, C.-W.; Lo, C.-L.; Chern, C.-S.; Chiu, H.-C. Tumor Microenvironment-Responsive Nanoparticle Delivery of Chemotherapy for Enhanced Selective Cellular Uptake and Transportation within Tumor. *Biomacromolecules* **2016**, *17*, 3883−3892.

(61) Chu, D.; Gao, J.; Wang, Z. Neutrophil-Mediated Delivery of Therapeutic Nanoparticles across Blood Vessel Barrier for Treatment of Inflammation and Infection. *ACS Nano* **2015**, *9*, 11800−11811.

(62) Giovinazzo, H.; Kumar, P.; Sheikh, A.; Brooks, K. M.; Ivanovic, M.; Walsh, M.; Caron, W. P.; Kowalsky, R. J.; Song, G.; Whitlow, A.; Clarke-Pearson, D. L.; Brewster, W. R.; Van Le, L.; Zamboni, B. A.; Bae-Jump, V.; Gehrig, P. A.; Zamboni, W. C. Technetium Tc 99m Sulfur Colloid Phenotypic Probe for the Pharmacokinetics and Pharmacodynamics of PEGylated Liposomal Doxorubicin in Women with Ovarian Cancer. *Cancer Chemother. Pharmacol.* **2016**, *77*, 565−573.

(63) Song, G.; Petschauer, J.; Madden, A.; Zamboni, W. Nanoparticles and the Mononuclear Phagocyte System: Pharmacokinetics and Applications for Inflammatory Diseases. *Curr. Rheumatol. Rev.* **2014**, *10*, 22−34.

(64) van der Meel, R.; Sulheim, E.; Shi, Y.; Kiessling, F.; Mulder, W. J. M.; Lammers, T. Smart Cancer Nanomedicine. *Nat. Nanotechnol.* **2019**, *14*, 1007−1017.

(65) Pérez-Medina, C.; Abdel-Atti, D.; Zhang, Y.; Longo, V. A.; Irwin, C. P.; Binderup, T.; Ruiz-Cabello, J.; Fayad, Z. A.; Lewis, J. S.; Mulder, W. J. M.; Reiner, T. A Modular Labeling Strategy for *In Vivo* PET and Near-Infrared Fluorescence Imaging of Nanoparticle Tumor Targeting. *J. Nucl. Med.* **2014**, *55*, 1706−1711.

(66) Holland, J. P.; Sheh, Y.; Lewis, J. S. Standardized Methods for the Production of High Specific-Activity Zirconium-89. *Nucl. Med. Biol.* **2009**, *36*, 729−739.

(67) Seynhaeve, A. L. B.; ten Hagen, T. L. M. Intravital Microscopy of Tumor-Associated Vasculature Using Advanced Dorsal Skinfold Window Chambers on Transgenic Fluorescent Mice. *J. Visualized Exp.* **2018**, *131*, No. e55115.